Nano Research

ISSN 1998-0124 CN 11-5974/O4
https://doi.org/10.1007/s12274-024-6812-1

Research Article

Approaching high oxygen evolution reaction performance by synergetic dual-ion leaching

Hancheng Ma[1], Yao Ding[1] (✉), Jianqi Li[1], Wei Peng[1], and Liqiang Mai[2]

[1] School of Materials Science and Engineering, Wuhan University of Technology, Wuhan 430070, China
[2] State Key Laboratory of Advanced Technology for Materials Synthesis and Processing, Wuhan University of Technology, Wuhan 430070, China

Received: 5 April 2024 / **Revised:** 15 May 2024 / **Accepted:** 3 June 2024

ABSTRACT

Self-reconstruction of catalysts during oxygen evolution reaction (OER) is crucial for the development of energy conversion technologies. However, the relationship between the specific atomic structure of pre-catalysts and their electrocatalytic behavior after reconstruction via dual-ion leaching has not been extensively researched. In this work, we design a highly effective non-noble metal OER catalyst with heterointerface through continuous self-reconstruction of $Co_2(OH)_3Cl$@$NiMoO_4$ as pre-catalyst by a straightforward dual-ion (i.e. MoO_4^{2-} and Cl^-) leaching. *In-situ* Raman and *in-situ* Fourier transform infrared (FT-IR) spectroscopy have precisely identified the progressive phase transformation of the pre-catalyst during self-reconstruction, which results in a stable heterojunction of CoOOH and NiOOH (CoOOH@NiOOH). Further calculations based on density functional theory (DFT) of CoOOH@NiOOH evident that more electrons will be aggregated in the Fermi level of Co. Notably, Gibbs free energy (ΔG) for different OER steps of CoOOH@NiOOH exhibit lower energy costs of all intermediates, implying the well catalytic properties. Ultimately, the catalyst derived from dual-ion leaching displays outstanding OER performance, characterized by an overpotential of 275 mV at a current density of 10 $mA{\cdot}cm^{-2}$ and exceptional stability over 12 h reaction. This work successfully paves a way of finding high-performance OER catalysts based on non-noble metal through dual-ion leaching during self-reconstruction.

KEYWORDS

dual-ion leaching, oxygen evolution reaction, chemical reconstruction, $NiMoO_4$, $Co_2(OH)_3Cl$

1 Introduction

In the quest for efficient and sustainable energy conversion technologies, the investigation of the oxygen evolution reaction (OER) has garnered considerable interest due to its pivotal role in water splitting, offering potential for clean energy generation [1–3]. The most effective OER electrocatalysts are noble metals and their oxides, e.g., IrO_2 and RuO_2 [4–6]. However, the natural scarcity and high costs of noble metals greatly limit the practical implementation. Nowadays, developing efficient catalysts based on non-noble metals (e.g., Mo, Ni, Co) and carefully exploring their involved mechanisms during OER are highly desirable and have been the main focus for researchers [7]. For some non-noble catalysts (e.g., $NiMoO_4$, $Co_2(OH)_3Cl$, $LaNiO_3$, Co_3O_4, etc.), also named as pre-catalysts, drastic self-reconstruction will occur during OER when achieving the oxidation potentials [1, 8, 9]. This leads to the formation of self-assembled metal oxy(hydroxide) layers with high catalytic activity on the surface of these pre-catalysts [10–13]. Although the derived high-valence metal oxy(hydroxide) active layers have been considered as true active species, it still cannot fully explain why pre-catalysts with diverse oxidation states display different atomic structures after self-reconstruction and derive varied catalytic activities [1]. Therefore, precisely identifying the atomic coordination of pre-catalysts and detecting the formation process of their intermediate products from reconstruction in real time is crucial to understanding the mechanism of OER based on non-noble metals [14, 15].

Recently, several researches have reported that the dynamic surface self-reconstruction will happen in some catalysts through an ionic leaching process, which is a key of boosting their OER activities [1, 8, 9]. For example, cobalt oxychloride ($Co_2(OH)_3Cl$) was found by Jiang et al. that the reconstruction delivers remarkable performance of 300 mV overpotential at a current density of 10 $mA{\cdot}cm^{-2}$ through the leaching of Cl ions [1]. $NiMoO_4$ was also rationally selected as the pre-catalyst due to its proven post OER structure from reconstruction [16]. Liu et al. explored the deeply reconstructed catalyst from $NiMoO_4$ with sufficient active species (NiOOH), and achieved high-mass-activity catalysis [17]. Mai et al. also uncovered the thermally induced complete reconstruction of molybdate pre-catalysts showed excellent OER performance [16]. Besides, several researches show that oxyhydroxide heterostructures are expected to enhance the reaction kinetics in OER, which is usually beneficial from the hydrophilic surface, the alternative electronic structure and the special adsorption/desorption ability of intermediates [18, 19]. However, limited efforts are devoted into designing pre-catalysts which can derive highly active heterostructures for OER through controllable reconstruction [20].

More importantly, the transformations in electronic and atomic

Address correspondence to ydingaf@whut.edu.cn

structure of pre-catalysts occur during OER reconstruction will significantly influence the oxidation states of intermediate species, which closely correlates to their catalytic performance. However, traditional *ex-situ* techniques are inadequate for comprehending the actual evolution of electronic and atomistic structures during reconstruction. In this case, *in-situ* techniques, e.g., *in-situ* Raman, *in-situ* Fourier transform infrared (FT-IR) spectroscopy, etc., are essential for uncovering the real-time structure transformation, as well as providing the information on kinetics of the reconstruction and revealing the mechanisms [21, 22]. Nowadays, some reported works have shown that *in-situ* techniques are powerful tools for understanding the structure evolution of catalytically active components from pre-catalysts with typical self-reconstruction [23]. For example, Vomiero et al. reported that in the core–shell structure of $NiMoO_4$ microrods covered by Co_3O_4 nanoparticles, Mo leaching is conductive to the reconstruction of pre-catalyst for active sites with high catalytic activity confirmed by *in-situ* Raman [24]. Liu et al. also applied analyses of *in-situ* X-ray absorption fine structure (XAFS) spectroscopy manifest that V sites of Ni-based metal-organic framework nanosheet arrays (NiV-MOF NAs) continuously accept electrons from the adjacent active Ni sites to promote OER kinetics [25]. Zhang et al. applied *in-situ* Raman in showing the initiates potential of $La_{1-x}Ce_xNiO_3$ during surface reconstruction in OER process [8]. Therefore, it is crucial for effectively employing *in-situ* techniques in teasing out the relationship between structural changes and the evolution of active sites during reconstruction by ionic leaching.

In this work, we cultivate a simple method to obtain a high-performance OER pre-catalyst based on $Co_2(OH)_3Cl$@$NiMoO_4$ which will provide stable and active heterointerfaces (CoOOH@NiOOH) derived from continuous self-reconstruction via synergetic dual-ion leaching. *In-situ* Raman and *in-situ* FT-IR techniques, combined with scanning transmission electron microscopy (STEM), are conducted to precisely identify the synergistic formation of CoOOH and NiOOH during the reconstruction. Further calculations based on density functional theory (DFT) of CoOOH@NiOOH evident that more electrons will be aggregated in the Fermi level of Co. Gibbs free energy (ΔG) for different OER steps of CoOOH@NiOOH exhibit lower energy costs of all intermediates, implying the well catalytic activity. By forming the heterostructures through dual-ion leaching, the catalysts show excellent and stable OER catalytic performance, featured by an overpotential of 275 mV at the current density of 10 $mA{\cdot}cm^{-2}$ and no obvious potential change during 12 h stability test.

2 Result and discussion

$Co_2(OH)_3Cl$@$NiMoO_4$ nanorods are obtained via a facial hydrothermal method followed by string with Co sources and propylene oxide (PO) to obtain the uniformly loaded of $Co_2(OH)_3Cl$ (details in Experimental). Figure 1(a) is the schematic diagram of a typical synthesis. Firstly, Na_2MoO_4 and $Ni(NO_3)_2$ are used as precursors for synthesizing $NiMoO_4$ nanorods, for which the detailed morphology is presented in Figs. S1 and S2 in the Electronic Supplementary Material (ESM). The $Co_2(OH)_3Cl$ are readily synthesized and loaded on the $NiMoO_4$ nanorods by a PO-initiated precipitation in the ethanol solution. In the precipitation, PO acts as a proton scavenger by protonating the epoxide oxygen and subsequently undergoing a ring-opening reaction [1].

This results in an increase in the pH value, which can facilitate the hydrolysis of metal ion aqueous complexes and lead to the

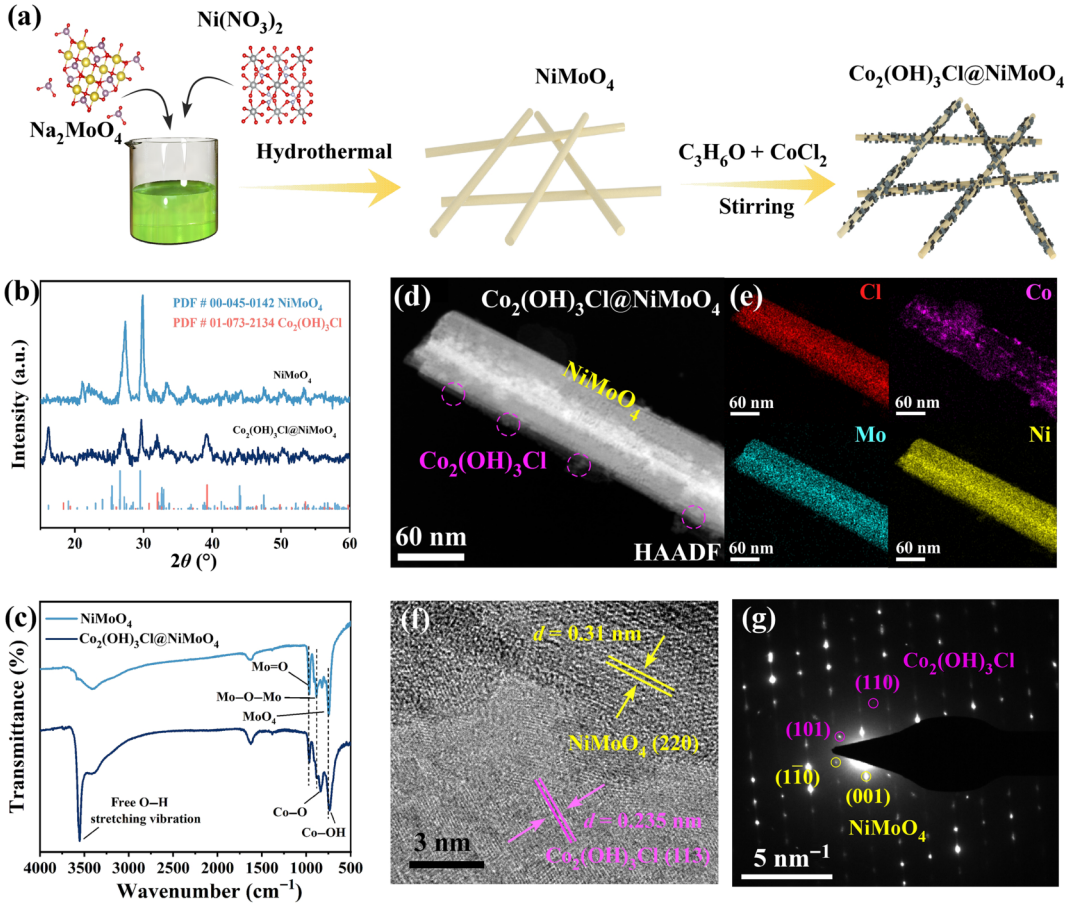

Figure 1 Synthesis and characterizations of $Co_2(OH)_3Cl$@$NiMoO_4$. (a) Schematic illustration of the synthesis for $Co_2(OH)_3Cl$@$NiMoO_4$. (b) XRD results and (c) FT-IR spectra for $Co_2(OH)_3Cl$@$NiMoO_4$. (d) HAADF-STEM and (e) corresponding elemental mapping images of $Co_2(OH)_3Cl$@$NiMoO_4$. (f) HRTEM image and (g) SAED indexed patterns of $Co_2(OH)_3Cl$ and $NiMoO_4$.

formation of $Co_2(OH)_3Cl$ [1]. To further prove the successful synthesis of $Co_2(OH)_3Cl$@$NiMoO_4$, X-ray diffraction (XRD) techniques (Fig. 1(b)) and the FT-IR spectroscopy (Fig. 1(c)) are used to characterize the products as received. In Fig. 1(b), the presence of well-defined and sharp diffractions within a 2θ range of 20°–80° confirms the highly crystallized structure of $Co_2(OH)_3Cl$@$NiMoO_4$ by comparing with $NiMoO_4$. Specifically, the diffractions obtained for $Co_2(OH)_3Cl$@$NiMoO_4$ can be well correlated to the index of $NiMoO_4$ (PDF No.00-045-0142) and $Co_2(OH)_3Cl$ (PDF No.01-073-2134), which confirms the formation of the $Co_2(OH)_3Cl$ in $Co_2(OH)_3Cl$@$NiMoO_4$ by this approach. In the fingerprint region of FT-IR spectra, the band at 959 cm^{-1} corresponds to the symmetrical stretching of M=O bonds [26], while the bands at 821 and 889 cm^{-1} correspond to the stretching vibration of Mo–O–Mo bonds [26, 27]. Additionally, the sharp band at 747 cm^{-1} is attributed to the bending vibration of the distorted MoO_4 units in both $Co_2(OH)_3Cl$@$NiMoO_4$ and $NiMoO_4$ [26]. For the FT-IR spectrum of $Co_2(OH)_3Cl$@$NiMoO_4$, all the above chemical bonds of $NiMoO_4$ can be observed, and the prominent band observed at 3550 cm^{-1} can be attributed to the free O–H stretching vibration in metal hydroxide layers [28–30]. Besides, both the FT-IR spectra of $Co_2(OH)_3Cl$@$NiMoO_4$ and $NiMoO_4$ show broad bands at 3374 and 1634 cm^{-1}, which refers to the surface-adsorbed water molecules [1]. The bands observed at 854 and 758 cm^{-1} are attributed to the Co–O bond and Co–OH bonds in $Co_2(OH)_3Cl$@$NiMoO_4$, respectively [29]. These XRD and infrared results provide solid evidences of the successful loading of $Co_2(OH)_3Cl$ on $NiMoO_4$ and the chemical environment in $Co_2(OH)_3Cl$@$NiMoO_4$.

To further observe the atomic structure of $Co_2(OH)_3Cl$@$NiMoO_4$, high angle annular dark-field STEM (HAADF-STEM) is used to analyze the detailed morphology and the elemental distribution of $Co_2(OH)_3Cl$@$NiMoO_4$. Figure 1(d) clearly depicts the $NiMoO_4$ nanorods with $Co_2(OH)_3Cl$ located at surface. Figure 1(e) is the corresponding energy dispersive X-ray (EDX, details in Fig. S3 in the ESM) elemental mapping images of Cl, Co, Mo and Ni in $Co_2(OH)_3Cl$@$NiMoO_4$, respectively. It indicates that Co mainly distributes at the surface, while Cl evenly distributes in the inner of nanorods, corresponding to the distribution of Co. The lattice spacing of $NiMoO_4$ and $Co_2(OH)_3Cl$ are measured respectively in Fig. 1(f). Here, lattice spacing d = 0.31 nm matches with the $NiMoO_4$ (220) lattice fringes, while d = 0.235 nm corresponding to $Co_2(OH)_3Cl$ (113). Furthermore, the selected area electron diffraction (SAED) patterns from the area in Fig. 1(f) show highly defined spots of different phases of $NiMoO_4$ and $Co_2(OH)_3Cl$ polycrystals (Fig. 1(g)).

The phase states of different elements in $Co_2(OH)_3Cl$@$NiMoO_4$ and $NiMoO_4$ are identified by X-ray photoelectron spectroscopy (XPS) in Fig. 2. The Mo 3d spectra of $Co_2(OH)_3Cl$@$NiMoO_4$ and $NiMoO_4$ (Fig. 2(a)) both exhibit dual peaks at around 236.2 and 233 eV, which can be attributed to the Mo $3d_{3/2}$ and $3d_{5/2}$ orbitals, respectively. The energy gap between these peaks is measured to be ~ 3.2 eV, indicating the presence of Mo^{6+} oxidation state in them [31]. At meantime, in $Co_2(OH)_3Cl$@$NiMoO_4$, due to the formation of new bonds between $Co_2(OH)_3Cl$ and $NiMoO_4$, the Mo $3d_{5/2}$ peak shifts towards higher binding energy (~ 0.2 eV). In Fig. 2(b), two peaks at 856.8 and 862.6 eV of $Co_2(OH)_3Cl$@$NiMoO_4$ and $NiMoO_4$ belong to Ni $2p_{3/2}$ and $2p_{1/2}$, respectively. Besides, the Ni 2p spectra exhibit two satellite peaks at 862.5 and 880.3 eV, respectively, corresponding to the oxidation states of Ni^{3+} and Ni^{2+} [31]. Here, no peak offset is detected in Ni 2p after loading $Co_2(OH)_3Cl$ compared with Mo 3d, which is probably the result of the coordination of Co and O for rather than the coordination of Mo or Ni. As shown in Fig. 2(c), Co 2p spectrum of $Co_2(OH)_3Cl$@$NiMoO_4$ can be fitted with two spin-orbit doublets and two shake-up satellites as well. The predominant valence state of the Co species in $Co_2(OH)_3Cl$@$NiMoO_4$ is determined to be +2 verified by Co $2p_{1/2}$ and Co $2p_{3/2}$ peaks located at 783.1 and 798.5 eV, respectively [1, 32]. Also, other satellite peaks indicate the presence of Co^{3+}. Moreover, in Fig. 2(d), the binding energy of Cl $2p_{3/2}$ (198.8 eV) and Cl $2p_{1/2}$ (200.7 eV) in $Co_2(OH)_3Cl$@$NiMoO_4$ is commonly

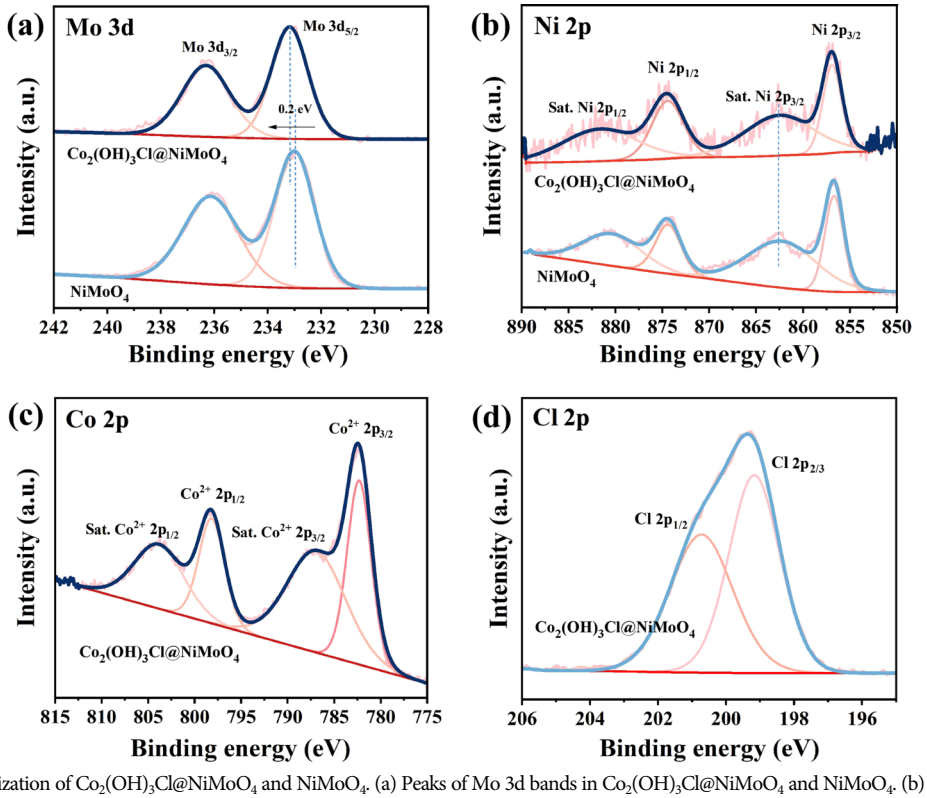

Figure 2 XPS characterization of $Co_2(OH)_3Cl$@$NiMoO_4$ and $NiMoO_4$. (a) Peaks of Mo 3d bands in $Co_2(OH)_3Cl$@$NiMoO_4$ and $NiMoO_4$. (b) Peaks of Ni 2p bands in $Co_2(OH)_3Cl$@$NiMoO_4$ and $NiMoO_4$. (c) Peaks of Co 2p bands in $Co_2(OH)_3Cl$@$NiMoO_4$. (d) Peaks of Cl 2p bands in $Co_2(OH)_3Cl$@$NiMoO_4$.

attributed to the lattice Cl^- [33]. No obvious O vacancy signal is detected in the O 1s spectrum (Fig. S4 in the ESM) [34].

Figure 3 validates the catalytic properties of $Co_2(OH)_3Cl@NiMoO_4$ in OER as the pre-catalysts. For test, $Co_2(OH)_3Cl@NiMoO_4$ is drop-casted onto a glassy carbon (GC) electrode and subjected to electrochemical measurements calibrated with reversible hydrogen electrode (RHE) scale and *iR*-correction in a 1.0 M KOH solution (see the ESM). All the loading of catalysts on GC electrodes is ~ 0.398 mg·cm^{-2}. In the linear sweep voltammetry (LSV) of $NiMoO_4$, the peak at around 1.36 V refers to the Ni oxidation [35]. Meanwhile, the peak at around 1.34 V of $Co_2(OH)_3Cl@NiMoO_4$ refers to the Ni and Co oxidation, shown in Fig. 3(a). Simultaneously, the optimal loading amount is found through various electrochemical tests (Fig. S6 in the ESM). Impressively, $Co_2(OH)_3Cl@NiMoO_4$ shows a remarkable activity of an overpotential of 275 mV at the current density (j) of 10 mA·cm^{-2}, which is much better than that of $NiMoO_4$ (340 mV), and even exceeds the property of commercial RuO_2 (280 mV). Besides, the Co content (23 wt.%) in $Co_2(OH)_3Cl@NiMoO_4$ is tested by inductively coupled plasma (ICP) and the mass activity of Co is calculated and shown in Fig. S7 in the ESM. Noteworthily, Fig. 3(b) calculates the Tafel slope of $Co_2(OH)_3Cl@NiMoO_4$, $NiMoO_4$ and commercial RuO_2, which results in the much lower slope as 62 mV·dec^{-1} for $Co_2(OH)_3Cl@NiMoO_4$, compared with that of $NiMoO_4$ (118 mV·dec^{-1}) and commercial RuO_2 (89 mV·dec^{-1}). This indicates the improved kinetics of $Co_2(OH)_3Cl@NiMoO_4$ towards OER. Electrochemical impedance spectroscopy (EIS) is a valuable technique that can offer further insights into the relationship between the structure and reaction kinetics of $Co_2(OH)_3Cl@NiMoO_4$. Nyquist plots (Fig. 3(c)) show the well pronounced charge-transfer resistance (R_{ct}) for $Co_2(OH)_3Cl@NiMoO_4$ (9.1 Ω) which is smaller than that of $NiMoO_4$ (51.2 Ω) and commercial RuO_2 (38.5 Ω). These results verify that the formation of heterogeneous structure of $Co_2(OH)_3Cl@NiMoO_4$ can accelerate the electron transfer efficiency during OER. The double-layer capacitances (C_{dl}) of $Co_2(OH)_3Cl@NiMoO_4$ also exhibit more effective adsorption behavior (Fig. S8 in the ESM). Furthermore, Figs. 3(d) and 3(e) statistically present the overpotential and Tafel slope of $Co_2(OH)_3Cl@NiMoO_4$, $NiMoO_4$, RuO_2 and other pioneer works based on $NiMoO_4$ [36–41], which exhibits the exceptionally high catalytic properties of $Co_2(OH)_3Cl@NiMoO_4$ in this work (details in the ESM). Aim at observing the structural stability, current parameters (CP) durability is evaluated with the current density j = 10 mA·cm^{-2} in Fig. 3(f). At beginning, an obvious enhancement of the activity is observed, which should be caused by the Mo and Cl species leaching in OER, verified by the following characterizations in this work. This implies that the reconstruction is the key of the boosting the catalytic activity of $Co_2(OH)_3Cl@NiMoO_4$. In addition, $Co_2(OH)_3Cl@NiMoO_4$ also exhibits promising repeatability of 5 mV changed overpotential obtained at 10 mA·cm^{-2} (Fig. S9 in the ESM).

To confirm the above inference, the concentration of Cl^- in the electrolyte is detected by reacting with an $AgNO_3$ solution in the presence of excess HNO_3 (details in the ESM). Figure 3(f) also shows that with the continuous OER (within 12 h), an increasing amount of AgCl precipitates is observed in the extracted

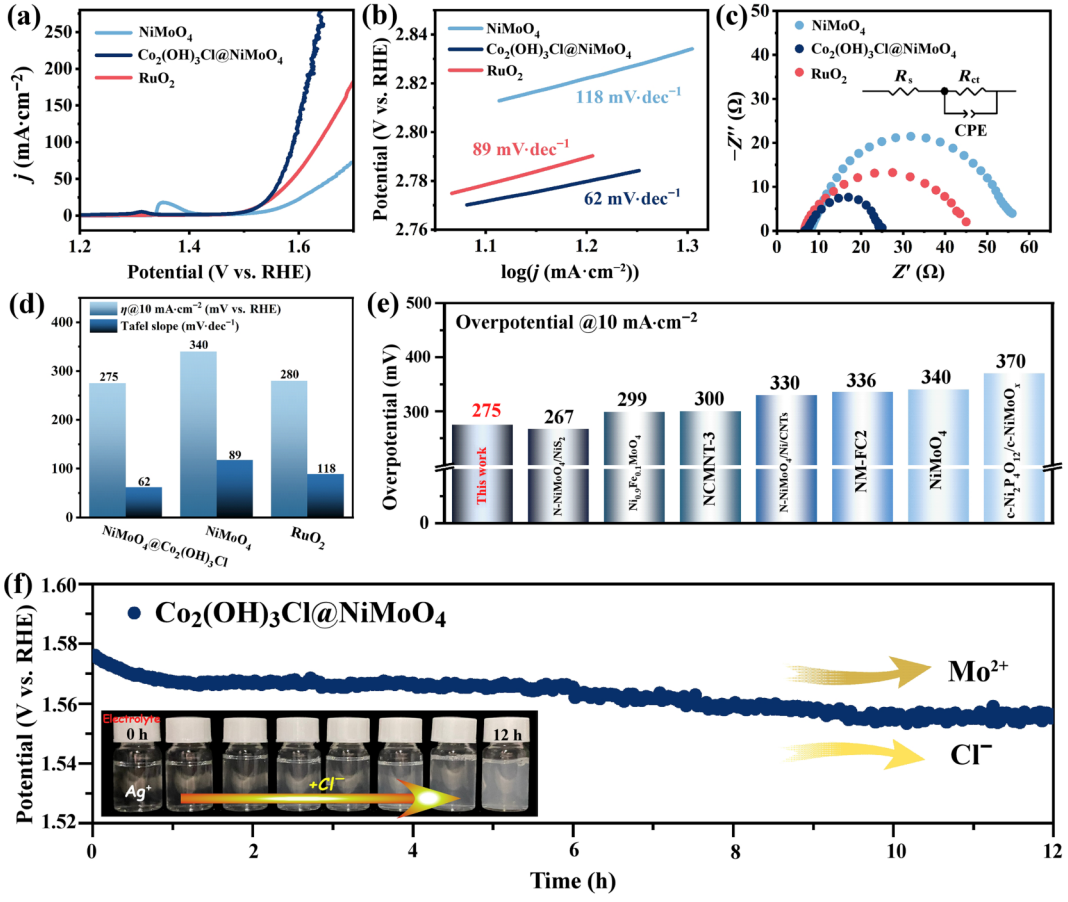

Figure 3 OER performance of $Co_2(OH)_3Cl@NiMoO_4$. (a) OER polarization curves and (b) corresponding Tafel plots of $Co_2(OH)_3Cl@NiMoO_4$ and $NiMoO_4$. (c) Nyquist plots of $Co_2(OH)_3Cl@NiMoO_4$ and $NiMoO_4$ at the overpotential of 10 mV. (d) Overpotential and Tafel slope performance comparation histogram of different electrodes. (e) Overpotential performance comparation histogram of $NiMoO_4$-based OER catalysts reported in recent years. (f) Stability test of $Co_2(OH)_3Cl@NiMoO_4$ via chronoamperometry with optical images for the electrolyte with AgCl during the increase time, which can indicate the concentration of Cl^- electrolyte derived from reconstruction of $Co_2(OH)_3Cl$.

electrolyte. This observation effectively demonstrates that the OER process should lead to the Cl^- species leaching.

To fully understand the structure and formation changes during the *in-situ* Raman characterization of $Co_2(OH)_3Cl$@$NiMoO_4$ are conducted to give an intuitive illustration of the enhancement of catalytic properties. *In-situ* FT-IR in the range of 650–2000 cm^{-1} showed by Figs. 4(a) and 4(b) are performed to support the chemical environment changes in electrodes and electrolyte during the reconstruction. Time-resolved *in-situ* FT-IR spectroscopy in 1.0 M KOH without any applied bias reveals the instantaneous disappearance of $Co_2(OH)_3Cl$ and appearance of CoOOH. For details, the peak at 1625 cm^{-1} is the characteristic peak of CoOOH with Co=O bonds in the crystal structure, and the band at 855 cm^{-1} is attributed to the Co–O bond in the CoOOH [29, 42]. During the OER, a noticeable enhancement in the signal of Co=O and Co–O bonds is observed which proves the transformation from $Co_2(OH)_3Cl$ to CoOOH caused by Cl^- leaching. Moreover, the intensity enhancement of Mo=O bond at 985 cm^{-1} should come from the leaching of MoO_4^{2-} derived from the reconstruction of $NiMoO_4$, and then dissolved into the electrolyte. Furthermore, for *in-situ* Raman spectra in Figs. 4(c) and 4(d), the instantaneous disappearance of the $NiMoO_4$ vibrations at 946, 851 and 353 cm^{-1} clearly shows the MoO_4^{2-} leaching and the structural collapse of $NiMoO_4$. Besides, the continuously enhanced signal at 470 cm^{-1} is attributed to the Ni–O bending vibration modes of γ-NiOOH [43–45]. Therefore, the above *in-situ* characterizations clearly depict that $Co_2(OH)_3Cl$@$NiMoO_4$ can simultaneously undergo the electrochemical reconstruction of dual-ion during the OER process. Furthermore, we have characterized the catalysts post OER and the final products are mainly composed of amorphous states NiOOH and partial crystalline CoOOH, which is consistent with previous results that the reconstruction of $NiMoO_4$ can result in the amorphous NiOOH (Figs. S10 and S11 in the ESM) [43].

In order to further illustrate the structure-catalytic activities of $Co_2(OH)_3Cl$@$NiMoO_4$ in OER through this dual-ion leaching reconstruction approach, the total and partial electronic density of states (TDOS and PDOS) of CoOOH@NiOOH, NiOOH and CoOOH are calculated in Figs. 5(a) and 5(b) (details of the calculations in the ESM). Here, CoOOH@NiOOH heterostructure is constructed as the active intermediate products during reconstruction in Fig. 5(c), verified in above discussions. Besides, post OER characterization demonstrates the presence of heterojunctions (Fig. S11 in the ESM) after reconstruction. By forming the heterostructures of CoOOH@NiOOH, its semi-metallic properties can be quite obvious from the results of DOS, which should be beneficial for the rapid transportation of electrons through heterointerface compared with bare CoOOH or NiOOH [46]. This result is further validated by EIS testing of CoOOH@NiOOH, CoOOH and NiOOH (Fig. S12 in the ESM).

Besides, from the calculations of PDOS, it can be seen that the electronic states near the Fermi level are mainly contributed by O while other states are mainly contributed by Ni and Co elements in CoOOH@NiOOH which shows the main active sites of the catalyst [47]. Notably, for CoOOH@NiOOH, the heterostructure can greatly enhance the electronic density around the Fermi level, which implies the high electric conductivity and better adsorption properties of protons [48]. Furthermore, to detailly observe the advantages of CoOOH@NiOOH heterostructures in different OER steps, the ΔG profiles for the OER pathway at the free energy

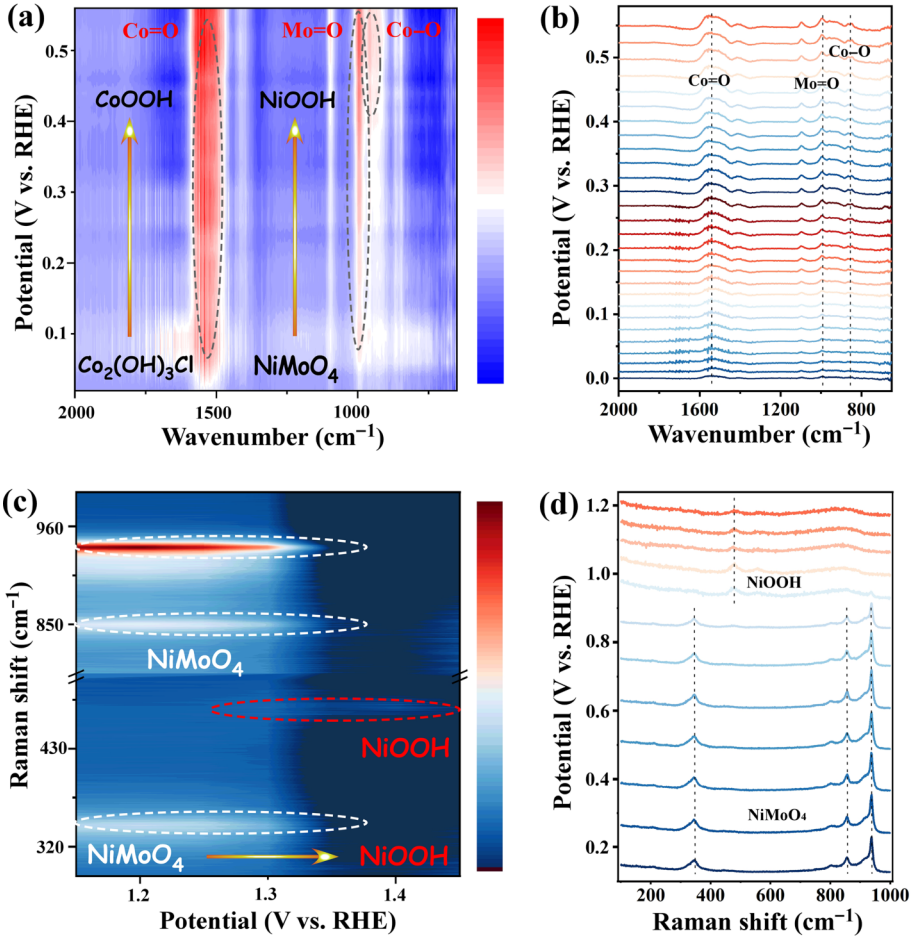

Figure 4 *In-situ* FT-IR and Raman characterization of $Co_2(OH)_3Cl$@$NiMoO_4$. (a) two-dimensional (2D) contour diagram and (b) referred line plot of *in-situ* FT-IR spectroscopy of $Co_2(OH)_3Cl$@$NiMoO_4$ in 1.0 M KOH during OER. (c) 2D contour diagram and (d) referred line plot of *in-situ* Raman spectroscopy without applied bias of $Co_2(OH)_3Cl$@$NiMoO_4$ in 1.0 M KOH during OER.

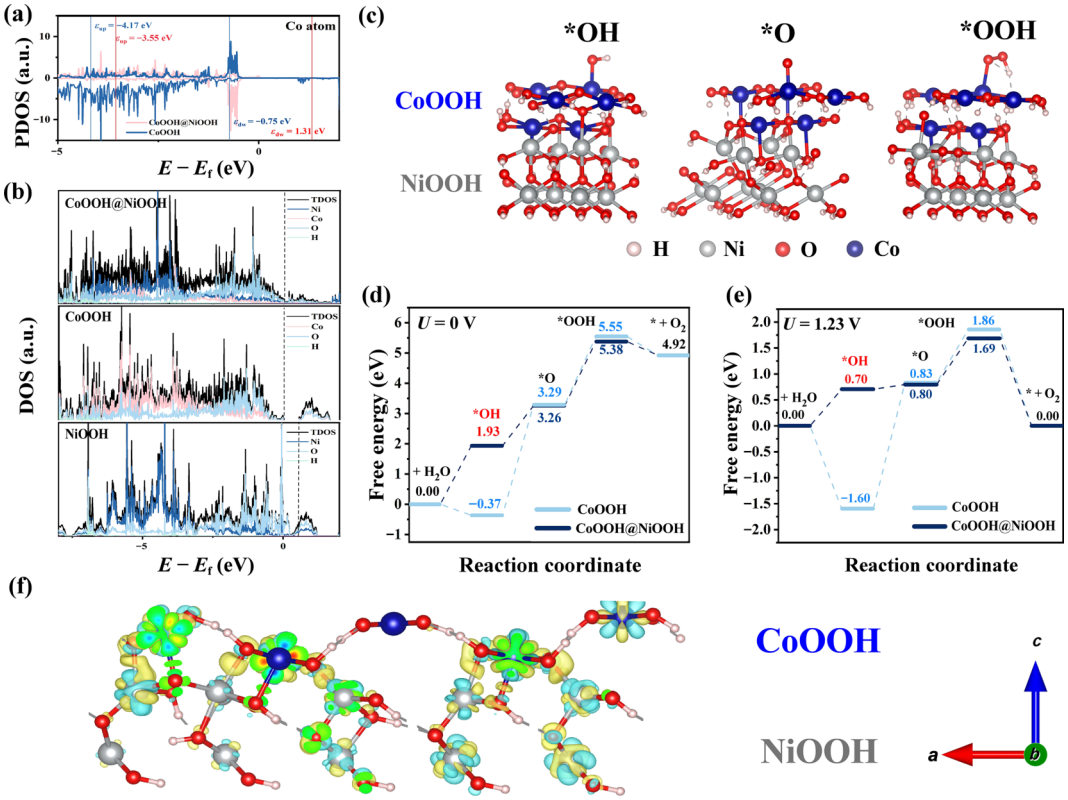

Figure 5 Theoretical DFT calculations for CoOOH@NiOOH during OER. ((a) and (b)) TDOS and PDOS of CoOOH@NiOOH, CoOOH and NiOOH. (c) Atomic structure of *OH, O* and *OOH absorbed on the surface of CoOOH@NiOOH during different steps in OER. ((d) and (e)) Profiles of calculated Gibbs free energy (d) U = 0 and (e) U = 1.23 for CoOOH@NiOOH and CoOOH during different steps in OER. (f) Charge density difference in the interface of CoOOH@NiOOH, the yellow and blue zones represent the charge accumulation or dispersion, respectively.

diagrams under different potential U = 0 and 1.23 for CoOOH@NiOOH and CoOOH are given in Figs. 5(d) and 5(e), respectively. Under alkaline conditions, OER involves four proton–electron transfer steps at active sites and results in the formation of three intermediates (*OH, *O and *OOH, * = active sites)

$$\text{Step 1}: OH^- + * \rightarrow *OH + e^-$$

$$\text{Step 2}: *OH + OH^- \rightarrow *O + H_2O + e^-$$

$$\text{Step 3}: *O + OH^- \rightarrow *OOH + e^-$$

$$\text{Step 4}: *OOH + OH^- \rightarrow * + O_2 + H_2O + e^-$$

For OER, it is theoretically posited that each electron step necessitates an external voltage of 1.23 V to facilitate the adsorption of hydrogen protons from the surface [49]. In the case of CoOOH@NiOOH, the third step exhibits the largest energy barrier of ΔG under the standard conditions (U = 0) and theoretical reaction conditions (U = 1.23), implying that the formation of *OOH on the surface of CoOOH@NiOOH is the potential determining step (PDS) for the OER process (Fig. 5(c)). These results indicate that *OOH adsorption tends to be the rate-limited step during the OER process, and the catalytic activity order is CoOOH@NiOOH > CoOOH because that ΔG of the *OOH adsorption intermediates are 5.38 and 5.55 at U = 0, 1.69 and 1.86 at U = 1.23, respectively. Notably, CoOOH@NiOOH exhibited all lower energy costs of *OH, *O and *OOH intermediates than the bare CoOOH, thus bringing its overall oxygen absorption energetics closer to Fermi level E_f ($|\Delta G_{*OOH}| \approx |\Delta G_{*OH}| \approx |\Delta G_{*O}|$\to0) [50]. Therefore, the above calculations further indicate that the special electronic structure of CoOOH@NiOOH heterointerfaces benefited from dual-ion leaching can contribute to the outstanding OER behavior. To understand the transport of carriers at the interface, we obtain the differential charge densities as shown in Fig. 5(f), with the yellow region and the cyan region denoting electron accumulation and electron depletion, respectively. It can be seen that there is obvious charge migration from NiOOH to CoOOH [51]. Besides, the Bader charge diagram for OER of CoOOH@NiOOH is calculated (Fig. S12 in the ESM) showing the direction of electronic transfer.

3 Conclusion

In conclusion, we have developed a unique pre-catalyst that exhibits continuous self-reconstruction and enhanced OER activities through the leaching of dual-ionic species. The active sites derived from this dual-ion leaching exhibit a special heterostructure of CoOOH@NiOOH which contributes to the highly active and stable performance in alkaline electrolytes. The structure of the derived active components and the kinetics of self-reconstruction are also identified by *in-situ* characterizations. Utilizing the dual-ion leaching, we have developed a theoretical model of the CoOOH@NiOOH heterostructure for DFT calculations. This model demonstrates that the dual-ion leaching results in a unique electronic structure, which in turn enhances the catalytic activities and stability of the catalyst. The strategy of dual-ion leaching established in this work can provide a reference for designing high-performance OER catalysts based on non-noble metals in future.

4 Experimental

4.1 Synthesis of $NiMoO_4$ nanorods

For the synthesis of $NiMoO_4$ nanorods, a mixture solution of

Na_2MoO_4 (0.3 mmol) and $Ni(NO_3)_2$ (0.3 mmol) was dissolved in ultrapure water (50 mL), and then transferred into a 100 mL Teflon-lined stainless-steel autoclave. The vessel was heated for 6 h at a temperature of 180 °C. After the autoclave was left to cool down, $NiMoO_4$ nanorods were collected.

4.2 Synthesis of $Co_2(OH)_3Cl$@$NiMoO_4$

For the synthesis of $Co_2(OH)_3Cl$@$NiMoO_4$, 50 mg of as received $NiMoO_4$ powder was dispersed in 9 mL ethanol, different amount of $CoCl_2$ (0.2, 0.4, 0.6, 0.7, 0.8 and 1 mmol) together with 2.6 mL ethylene oxide were prepared with 12 h stirring to obtain the samples and the best catalytic property.

4.3 Characterizations

The XRD test was characterized by a Bruker D8 Discover X-ray diffractometer (XRD) equipped with a Cu Kα radiation source and Raman spectra were carried out by using a HORIBA HR EVO Raman system with a 532 nm laser. TEM, HAADF-STEM and high-resolution TEM (HRTEM) images, together with the SAED patterns and EDX mapping, were conducted with Talos F200S and Themis Z (3.2) operating at 200 KV. Scanning electron microscopy (SEM) images were carried out by a JEOL-7100F scanning electron microscope. XPS was performed using ESCALAB 250Xi.

4.4 Measurements of OER properties

The electrochemical measurements were performed on the CHI760E electrochemical workstation with a standard three-electrode system at room temperature (25 °C). A GC electrode (GCE, diameter: 4 mm, geometric area: 0.1256 cm^2), a carbon rod and a Hg-HgO electrode were used as the working, counter and reference electrodes, respectively. The electrolyte was made of 1 M KOH solution saturated by argon. The GCE was polished with Al_2O_3 slurry before loading catalysts to obtain a clean smooth surface. Subsequently, 5 mg of catalysts and 5 mg Vulcan XC-72R were dispersed in 800 μL of isopropanol and 150 μL pure water with 50 μL of Nafion solution (5 wt.%) and then sonicated for 15 min to obtain a homogeneous catalyst ink which 10 μL was dropped onto the GCE and placed dry at room temperature. The LSV curves were collected at a sweep rate as 5.0 $mV \cdot s^{-1}$ with 70% of ohmic drop compensation. The electrolyte of the calomel electrode was filled with saturated potassium chloride solution and replaced weekly. EIS measurements were conducted at an overpotential as 10 mV in the frequency range from 0.01 to 10^5 Hz with an amplitude of 5 mV. The chronograph potentiometer parameter test was set to be tested at j = 10 $mA \cdot cm^{-2}$ for over 100 h. Samples after stability testing were collected by sonication. The polarization curves were corrected by iR compensation. The correction was performed according to the following equation

$$E_{corrected} = E_{measured} - iR_s \quad (1)$$

where the $E_{corrected}$, $E_{measured}$, i and R_s are the iR-corrected potential, the measured potential vs. RHE, the current, and the internal resistance acquired by the EIS, respectively.

The electrolyte (1 mL) at different time moments of 0, 1, 2, 4, 6, 8, 10 and 12 h during the CP test in 1.0 M KOH was sucked out and added into a HNO_3-rich $AgNO_3$ solution (1 $mol \cdot L^{-1}$; 5 mL) to detect the relative Cl^- contents through the observation of insoluble AgCl precipitation.

4.5 Synthesis of $Co_2(OH)_3Cl$@$NiMoO_4$

The overpotential values were defined by the Tafel equation

$$\eta = \alpha + b\log|j| \quad (2)$$

where η is the applied overpotential, j is the current density, α is the value of the overpotential when the current density is equal to 1 $A \cdot cm^{-2}$, the Tafel slope (b) can be obtained.

Acknowledgements

This work was financially supported by the National Key Research and Development Program of China (No. 2023YFB3809301) and the National Natural Science Foundation of China (Nos. 61905183, 52127816 and 51832004).

Electronic Supplementary Material: Supplementary material (computational details and supporting information) is available in the online version of this article at https://doi.org/10.1007/s12274-024-6812-1.

References

[1] Jiang, H. L.; He, Q.; Li, X. Y.; Su, X. Z.; Zhang, Y. K.; Chen, S. M.; Zhang, S.; Zhang, G. Z.; Jiang, J.; Luo, Y. et al. Tracking structural self-reconstruction and identifying true active sites toward cobalt oxychloride precatalyst of oxygen evolution reaction. *Adv. Mater.* **2019**, *31*, 1805127.

[2] Zhang, K. X.; Zou, R. Q. Advanced transition metal-based OER electrocatalysts: Current status, opportunities, and challenges. *Small* **2021**, *17*, 2100129.

[3] Spöri, C.; Briois, P.; Nong, H. N.; Reier, T.; Billard, A.; Kühl, S.; Teschner, D.; Strasser, P. Experimental activity descriptors for iridium-based catalysts for the electrochemical oxygen evolution reaction (OER). *ACS Catal.* **2019**, *9*, 6653–6663.

[4] Daiane Ferreira da Silva, C.; Claudel, F.; Martin, V.; Chattot, R.; Abbou, S.; Kumar, K.; Jiménez-Morales, I.; Cavaliere, S.; Jones, D.; Rozière, J. et al. Oxygen evolution reaction activity and stability benchmarks for supported and unsupported IrO_x electrocatalysts. *ACS Catal.* **2021**, *11*, 4107–4116.

[5] Ma, Z.; Zhang, Y.; Liu, S. Z.; Xu, W. Q.; Wu, L. J.; Hsieh, Y. C.; Liu, P.; Zhu, Y. M.; Sasaki, K.; Renner, J. N. et al. Reaction mechanism for oxygen evolution on RuO_2, IrO_2, and RuO_2@IrO_2 core–shell nanocatalysts. *J. Electroanal. Chem.* **2018**, *819*, 296–305.

[6] Zhu, W. J.; Yao, F.; Cheng, K. J.; Zhao, M. T.; Yang, C. J.; Dong, C. L.; Hong, Q. M.; Jiang, Q.; Wang, Z. C.; Liang, H. F. Direct dioxygen radical coupling driven by octahedral ruthenium-oxygen-cobalt collaborative coordination for acidic oxygen evolution reaction. *J. Am. Chem. Soc.* **2023**, *145*, 17995–18006.

[7] Blasco-Ahicart, M.; Soriano-López, J.; Carbó, J. J.; Poblet, J. M.; Galan-Mascaros, J. R. Polyoxometalate electrocatalysts based on earth-abundant metals for efficient water oxidation in acidic media. *Nat. Chem.* **2018**, *10*, 24–30.

[8] Sun, Y.; Li, R.; Chen, X. X.; Wu, J.; Xie, Y.; Wang, X.; Ma, K. K.; Wang, L.; Zhang, Z.; Liao, Q. L. et al. A - site management prompts the dynamic reconstructed active phase of perovskite oxide OER catalysts. *Adv. Energy Mater.* **2021**, *11*, 2003755.

[9] Selvam, N. C. S.; Du, L. J.; Xia, B. Y.; Yoo, P. J.; You, B. Reconstructed water oxidation electrocatalysts: The impact of surface dynamics on intrinsic activities. *Adv. Funct. Mater.* **2021**, *31*, 2008190.

[10] Liu, J. Z.; Ji, Y. F.; Nai, J. W.; Niu, X. G.; Luo, Y.; Guo, L.; Yang, S. H. Ultrathin amorphous cobalt-vanadium hydr(oxy)oxide catalysts for the oxygen evolution reaction. *Energy Environ. Sci.* **2018**, *11*, 1736–1741.

[11] Chen, P. Z.; Xu, K.; Fang, Z. W.; Tong, Y.; Wu, J. C.; Lu, X. L.; Peng, X.; Ding, H.; Wu, C. Z.; Xie, Y. Metallic Co_4N porous nanowire arrays activated by surface oxidation as electrocatalysts for the oxygen evolution reaction. *Angew. Chem., Int. Ed.* **2015**, *54*, 14710–14714.

[12] Zhang, Y. K.; Wu, C. Q.; Jiang, H. L.; Lin, Y. X.; Liu, H. J.; He, Q.; Chen, S. M.; Duan, T.; Song, L. Atomic iridium incorporated in

cobalt hydroxide for efficient oxygen evolution catalysis in neutral electrolyte. *Adv. Mater.* **2018**, *30*, 1707522.

[13] Zeng, Y.; Zhao, M. T.; Huang, Z. H.; Zhu, W. J.; Zheng, J. X.; Jiang, Q.; Wang, Z. C.; Liang, H. F. Surface reconstruction of water splitting electrocatalysts. *Adv. Energy Mater.* **2022**, *12*, 2201713.

[14] Guo, D. Y.; Zeng, Z. H.; Wan, Z. X.; Li, Y.; Xi, B.; Wang, C. X. A CoN‐based OER electrocatalyst capable in neutral medium: Atomic layer deposition as rational strategy for fabrication. *Adv. Funct. Mater.* **2021**, *31*, 2101324.

[15] Gao, X. R.; Yu, Y.; Liang, Q. R.; Pang, Y. J.; Miao, L. Q.; Liu, X. M.; Kou, Z. K.; He, J. Q.; Pennycook, S. J.; Mu, S. C. et al. Surface nitridation of nickel-cobalt alloy nanocactoids raises the performance of water oxidation and splitting. *Appl. Catal. B: Environ.* **2020**, *270*, 118889.

[16] Liu, X.; Guo, R. T.; Ni, K.; Xia, F. J.; Niu, C. J.; Wen, B.; Meng, J. S.; Wu, P. J.; Wu, J. S.; Wu, X. J. et al. Reconstruction-determined alkaline water electrolysis at industrial temperatures. *Adv. Mater.* **2020**, *32*, e2001136.

[17] Liu, X.; Ni, K.; Wen, B.; Guo, R. T.; Niu, C. J.; Meng, J. S.; Li, Q.; Wu, P. J.; Zhu, Y. W.; Wu, X. J. et al. Deep reconstruction of nickel-based precatalysts for water oxidation catalysis. *ACS Energy Lett.* **2019**, *4*, 2585–2592.

[18] Xing, Y. C.; Liu, S. L.; Liu, Y.; Xiao, X. C.; Li, Y.; Wang, Z. Y.; Hu, Y. L.; Xin, B. W.; Wang, H.; Wang, C. Construction of nickel phosphide/iron oxyhydroxide heterostructure nanoparticles for oxygen evolution. *Nano Energy* **2024**, *123*, 109402.

[19] Zhou, M.; Weng, Q. H.; Zhang, X. Y.; Wang, X.; Xue, Y. M.; Zeng, X. H.; Bando, Y.; Golberg, D. *In situ* electrochemical formation of core–shell nickel-iron disulfide and oxyhydroxide heterostructured catalysts for a stable oxygen evolution reaction and the associated mechanisms. *J. Mater. Chem. A* **2017**, *5*, 4335–4342.

[20] Duan, Y.; Lee, J. Y.; Xi, S. B.; Sun, Y. M.; Ge, J. J.; Ong, S. J. H.; Chen, Y. B.; Dou, S.; Meng, F. X.; Diao, C. Z. et al. Anodic oxidation enabled cation leaching for promoting surface reconstruction in water oxidation. *Angew. Chem., Int. Ed.* **2021**, *60*, 7418–7425.

[21] Wygant, B. R.; Kawashima, K.; Mullins, C. B. Catalyst or precatalyst? The effect of oxidation on transition metal carbide, pnictide, and chalcogenide oxygen evolution catalysts. *ACS Energy Lett.* **2018**, *3*, 2956–2966.

[22] Zhou, P.; Lv, X. S.; Tao, S. S.; Wu, J. C.; Wang, H. F.; Wei, X. X.; Wang, T. H.; Zhou, B.; Lu, Y. X.; Frauenheim, T. et al. Heterogeneous-interface-enhanced adsorption of organic and hydroxyl for biomass electrooxidation. *Adv. Mater.* **2022**, *34*, 2204089.

[23] Jin, S. Are metal chalcogenides, nitrides, and phosphides oxygen evolution catalysts or bifunctional catalysts. *ACS Energy Lett.* **2017**, *2*, 1937–1938.

[24] Solomon, G.; Landström, A.; Mazzaro, R.; Jugovac, M.; Moras, P.; Cattaruzza, E.; Morandi, V.; Concina, I.; Vomiero, A. $NiMoO_4$@Co_3O_4 core–shell nanorods: *In situ* catalyst reconstruction toward high efficiency oxygen evolution reaction. *Adv. Energy Mater.* **2021**, *11*, 2101324.

[25] Sun, X.; Zhang, X. X.; Li, Y. L.; Xu, Y. Z.; Su, H.; Che, W.; He, J. F.; Zhang, H.; Liu, M. H.; Zhou, W. L. et al. *In situ* construction of flexible V–Ni redox centers over Ni-based MOF nanosheet arrays for electrochemical water oxidation. *Small Methods* **2021**, *5*, 2100573.

[26] Rajput, A.; Adak, M. K.; Chakraborty, B. Intrinsic lability of $NiMoO_4$ to excel the oxygen evolution reaction. *Inorg. Chem.* **2022**, *61*, 11189–11206.

[27] Aishwarya, K.; Maruthasalamoorthy, S.; Mani, J.; Anbalagan, G.; Nirmala, R.; Navaneethan, M.; Navamathavan, R. Structural formation of multifunctional $NiMoO_4$ nanorods for thermoelectric applications. *Phys. Chem. Chem. Phys.* **2022**, *24*, 25620–25629.

[28] Mansournia, M.; Rakhshan, N. Hydrothermal synthesis and tuning of size and morphology of α-$Co(OH)_2$ and α-$Co_2(OH)_3Cl$ nanostructures as precursors for nanosized Co_3O_4. *Ceram. Int.* **2017**, *43*, 7282–7289.

[29] Li, H. H.; Tan, M. Y.; Huang, C.; Luo, W. P.; Yin, S. F.; Yang, W. J. $Co_2(OH)_3Cl$ and MOF mediated synthesis of porous Co_3O_4/NC nanosheets for efficient OER catalysis. *Appl. Surf. Sci.* **2021**, *542*, 148739.

[30] Liu, X. H.; Qu, B. H.; Zhu, F. H.; Gong, L. Y.; Su, L. H.; Zhu, L. Q. Sonochemical synthesis of β-$Co(OH)_2$ hexagonal nanoplates and their electrochemical capacitive behaviors. *J. Alloys Compd.* **2013**, *560*, 15–19.

[31] Hussain, S.; Javed, M. S.; Asim, S.; Shaheen, A.; Khan, A. J.; Abbas, Y.; Ullah, N.; Iqbal, A.; Wang, M. S.; Qiao, G. J. et al. Novel gravel-like $NiMoO_4$ nanoparticles on carbon cloth for outstanding supercapacitor applications. *Ceram. Int.* **2020**, *46*, 6406–6412.

[32] Zhang, Z. R.; Du, W. M.; Ren, X. R.; Shen, Z. W.; Fan, X. Y.; Wei, S. H.; Wei, C. Z.; Cao, Z.; Zhang, B. $Ni(OH)_2$-$Co_2(OH)_3Cl$ bilayer nanocomposites supported by Ni foams for binder-free electrodes of high-performance hybrid supercapacitors. *Appl. Surf. Sci.* **2019**, *469*, 624–633.

[33] Zhang, Z. W.; Yin, L. W. Mn-doped $Co_2(OH)_3Cl$ xerogels with 3D interconnected mesoporous structures as lithium ion battery anodes with improved electrochemical performance. *J. Mater. Chem. A* **2015**, *3*, 17659–17668.

[34] Qing, C.; Yang, C. X.; Chen, M. Y.; Li, W. H.; Wang, S. Y.; Tang, Y. W. Design of oxygen-deficient $NiMoO_4$ nanoflake and nanorod arrays with enhanced supercapacitive performance. *Chem. Eng. J.* **2018**, *354*, 182–190.

[35] Suen, N. T.; Hung, S. F.; Quan, Q.; Zhang, N.; Xu, Y. J.; Chen, H. M. Electrocatalysis for the oxygen evolution reaction: Recent development and future perspectives. *Chem. Soc. Rev.* **2017**, *46*, 337–365.

[36] An, L.; Feng, J. R.; Zhang, Y.; Wang, R.; Liu, H. W.; Wang, G. C.; Cheng, F. Y.; Xi, P. X. Epitaxial heterogeneous interfaces on N‐$NiMoO_4$/NiS_2 nanowires/nanosheets to boost hydrogen and oxygen production for overall water splitting. *Adv. Funct. Mater.* **2019**, *29*, 1805298.

[37] Yin, Z. X.; Chen, Y. J.; Zhao, Y.; Li, C. Y.; Zhu, C. L.; Zhang, X. T. Hierarchical nanosheet-based $CoMoO_4$-$NiMoO_4$ nanotubes for applications in asymmetric supercapacitors and the oxygen evolution reaction. *J. Mater. Chem. A* **2015**, *3*, 22750–22758.

[38] Chen, J. Y.; Zhao, G. Q.; Chen, Y. P.; Rui, K.; Mao, H.; Dou, S. X.; Sun, W. P. Iron‐doped nickel molybdate with enhanced oxygen evolution kinetics. *Chem.—Eur. J.* **2019**, *25*, 280–284.

[39] Wang, Z. N.; Wang, H.; Ji, S.; Wang, X. Y.; Zhou, P. X.; Huo, S. H.; Linkov, V.; Wang, R. F. A high faraday efficiency $NiMoO_4$ nanosheet array catalyst by adjusting the hydrophilicity for overall water splitting. *Chem.—Eur. J.* **2020**, *26*, 12067–12074.

[40] Wang, J.; Hu, J.; Niu, S.; Li, S.; Du, Y.; Xu, P. Crystalline-amorphous $Ni_2P_4O_{12}$/$NiMoO_x$ nanoarrays for alkaline water electrolysis: Enhanced catalytic activity via *in situ* surface reconstruction. *Small* **2022**, *18*, 2105972.

[41] Li, G. L.; Qiao, X. Y.; Miao, Y. Y.; Wang, T. Y.; Deng, F. Synergistic effect of N-$NiMoO_4$/Ni heterogeneous interface with oxygen vacancies in N-$NiMoO_4$/Ni/CNTs for superior overall water splitting. *Small* **2023**, *19*, 2207196.

[42] Cudennec, Y.;. Lecerf, A. Étude du type structural de γ-$FeO(OH)_{(s)}$ et comparaison avec la structure de $Cu(OH)_{2(s)}$. *C. R. Acad. Sci. Ser. IIC Chem.* **2001**, *4*, 885–891.

[43] Dürr, R. N.; Maltoni, P.; Tian, H. N.; Jousselme, B.; Hammarström, L.; Edvinsson, T. From $NiMoO_4$ to γ-NiOOH: Detecting the active catalyst phase by time resolved *in situ* and *operando* Raman spectroscopy. *ACS Nano* **2021**, *15*, 13504–13515.

[44] Anantharaj, S.; Karthick, K.; Kundu, S. Evolution of layered double hydroxides (LDH) as high performance water oxidation electrocatalysts: A review with insights on structure, activity and mechanism. *Mater. Today Energy* **2017**, *6*, 1–26.

[45] Qiu, Z.; Tai, C. W.; Niklasson, G. A.; Edvinsson, T. Direct

observation of active catalyst surface phases and the effect of dynamic self-optimization in NiFe-layered double hydroxides for alkaline water splitting. *Energy Environ. Sci.* **2019**, *12*, 572–581.

[46] Wang, J. R.; Fan, Y. C.; Qi, S. Y.; Li, W. F.; Zhao, M. W. Bifunctional HER/OER or OER/ORR catalytic activity of two-dimensional $TM_3(HITP)_2$ with TM = Fe–Zn. *J. Phys. Chem. C* **2020**, *124*, 9350–9359.

[47] Zeng, L. Y.; Zhao, Z. L.; Huang, Q. Z.; Zhou, C. H.; Chen, W. X.; Wang, K.; Li, M. G.; Lin, F. X.; Luo, H.; Gu, Y. et al. Single-atom Cr–N_4 sites with high oxophilicity interfaced with Pt atomic clusters for practical alkaline hydrogen evolution catalysis. *J. Am. Chem. Soc.* **2023**, *145*, 21432–21441.

[48] Zhou, L. X.; Shao, Y. F.; Yin, F.; Li, J.; Kang, F. Y.; Lv, R. T. Stabilizing non-iridium active sites by non-stoichiometric oxide for acidic water oxidation at high current density. *Nat. Commun.* **2023**, *14*, 7644.

[49] Li, D. Y.; Zhang, A. D.; Feng, Z. Z.; Wang, W. T. Theoretical insights on the charge state and bifunctional OER/ORR electrocatalyst activity in 4d-transition-metal-doped g-C_3N_4 monolayers. *ACS Appl. Mater. Interfaces* **2024**, *16*, 5779–5791.

[50] Huang, H. J.; Yu, D. S.; Hu, F.; Huang, S. C.; Song, J. N.; Chen, H. Y.; Li, L. L.; Peng, S. J. Clusters induced electron redistribution to tune oxygen reduction activity of transition metal single-atom for metal-air batteries. *Angew. Chem., Int. Ed.* **2022**, *61*, e202116068.

[51] Zeng, Y.; Cao, Z.; Liao, J. Z.; Liang, H. F.; Wei, B. B.; Xu, X.; Xu, H. W.; Zheng, J. X.; Zhu, W. J.; Cavallo, L. et al. Construction of hydroxide pn junction for water splitting electrocatalysis. *Appl. Catal. B: Environ.* **2021**, *292*, 120160.